

https://dspace.org/

Entropy generation in CassonWilliamsonPowellEyring hybrid ferrofluid flow in a microchannel Adomian decomposition and deep neural networks approaches

Hammed A. Ogunseye; Y Tijani; S Oloniiju; Olumuyiwa Otegbeye; Titilayo Agbaje

SPRINGER
https://hdl.handle.net/10539/46291
WOS

Downloaded from a DSpace repository. https://dspace.org/

Colloid and Polymer Science (2025) 303:813–830
https://doi.org/10.1007/s00396-025-05384-w

RESEARCH

Entropy generation in Casson-Williamson-Powell-Eyring hybrid ferrofluid flow in a microchannel: Adomian decomposition and deep neural networks approaches

Hammed A. Ogunseye[1] · Yusuf O. Tijani[2] · Shina D. Oloniiju[2] · Olumuyiwa Otegbeye[3] · Titilayo M. Agbaje[3]

Received: 5 November 2024 / Revised: 9 January 2025 / Accepted: 27 January 2025 / Published online: 11 February 2025
© The Author(s) 2025

Abstract
Entropy generation is a fundamental concept in thermodynamics that measures the irreversibility of a process. Understanding the principles of entropy generation is crucial for optimizing thermal management and improving the efficiency of any thermal system. Its applications span a wide range, including heat exchangers, turbomachinery, chemical reactors, microfluidic devices, and many others. This study investigates the fluid flow and energy loss in the flow of three non-Newtonian fluids in a microchannel. The dynamical model incorporates the rheological behaviour of the three distinct fluids without the need for separate, independent mathematical models. These fluids Casson, Williamson, and Powell-Eyring are hybridized with a nanoparticle ferrofluid. The homogenization process is achieved using the Tiwari-Das model. Due to the magnetic body forces in the conservation of energy equation, the generation of entropy is taken into account from three sources: heat loss due to heat transfer, heat loss due to magnetic flow, and heat loss due to viscous dissipation. The solutions of the model equations are approximated using two solution techniques: the Adomian decomposition and deep neural network methods, and the results are compared with Maplesoft's fourth-order Runge–Kutta (RK4). The solutions of these three methodologies serve as benchmarks for each other. The solutions obtained from each method agree, thus validating the accuracy of the results. The study indicates that the Williamson fluid is the most sensitive to flow changes with varying Reynolds numbers. Although increasing the Reynolds number reduces flow rates near the wall to zero for all fluids, there is a transition near the upper region where higher Reynolds numbers enhance the flow rates of all fluids. Increasing the Brinkman number raises the entropy generation rate for all fluids while inversely affecting the Bejan number across all fluids. Adding more nanoparticles will impede fluid flow and enhance fluid heat transfer.

Keywords Entropy generation · Adomian decomposition · Neural network · Microchannel · Non-Newtonian fluids

Nomenclature

β	Casson fluid parameter
η	Similarity variable
Γ	Williamson fluid parameter
λ_1, λ_2	Eyring-Powell fluid parameters
μ	Dynamic viscosity
Ω	Temperature difference
ρ	Density
σ	Electrical conductivity
θ	Normalized temperature
b, c	Fluid constants
B_0	Uniform magnetic flux density
Be	Bejan number
Br	Brinkman number
c_p	Specific heat capacity
Ec	Eckert number
h	Length of the channel
Ha	Hartmann number
k	Thermal conductivity

✉ Yusuf O. Tijani
olodyusuf@gmail.com; yusuf.tijani@ru.ac.za

[1] West Virginia Academy, Al-Wukair, Doha, Qatar

[2] Department of Mathematics, Rhodes University, P.O. Box 94, Grahamstown 6140, South Africa

[3] School of Computer Science and Applied Mathematics, University of the Witwatersrand, Johannesburg, Private Bag 3, Braamfontein 2050, South Africa

N_s	Dimensionless entropy generation number
P	Axial pressure
Pe	Péclét number
Re	Reynolds number
S_G	Entropy generation
T	Hybrid nanofluid temperature
T_0	Ambient temperature
T_h	Wall temperature
u	Velocity
V_0	Uniform suction/injection velocity
We	Weissenberg number
y	Transversal coordinate
hnf	Hybrid nanofluid

Introduction

Recently, there has been a significant increase in the use and application of fluid-based substances and services. This trend reflects the growing role of fluids in various industries and technologies [1]. For example, COVID-19 vaccines were administered to the human body in liquid form, a fluid-type division. Silver is often applied as a fluid-like substance to create essential components such as printed circuit boards and touchscreens. Liquid metals are used in advanced technologies for improved heat dissipation [2]. It is, therefore, no exaggeration to recognize the widespread and essential role that fluids play in our daily lives. Researchers have focused on studying the practical and theoretical importance of fluids, including boundary layer flow and channel flow. Among these practical studies, fluid flow in channels is significant as it plays a key role in various engineering and industrial applications.

Channel flow refers to fluid movement through a confined space, such as a pipe, duct, or open channel like a riverbed [3]. This type of flow is bounded by solid surfaces, such as the walls of a pipe or the banks of a river. These boundaries influence the flow characteristics such as velocity distribution and pressure gradient. This flow type is common in engineering (combustion theory), environmental science, and various industries, where understanding fluid behaviour is critical for design and analysis. Ireka and Okoya [4] analyzed the channel flow of a second-grade fluid with power-law type viscosity variations. The study concluded that an increase in the spatial-dependent viscosity parameter results in an increased flow rate characterized by a more positive flow. They noted that the associated parabolic velocity profile is typical of low-viscosity fluids. Chinyoka [5] investigated the effect of viscoelasticity on a lubricant influenced by Arrhenius-type chemical reaction and shear forces, using the finite difference method for analysis. The study's finding showcased the advantages of viscoelastic fluids in the lubrication processes of thermally reactive lubricants, represented explicitly by the non-Newtonian (Oldroyd-B liquid), compared to Newtonian fluids. The analysis of Couette flow for an ionic fluid subjected to the effect of Hall effect in a micro channel was investigated by Das et al. [6]. The authors reported that a higher Hall parameter significantly boosts the velocity components.

Nazeer et al. [7] investigated the multi-dimensional flow of a third-grade fluid in an inclined channel, accounting for lubrication effects. The deterministic model proposed in the study highlighted the significant role of magnetic fields. According to the study, the flow in the steep channel was driven by gravitational forces. The authors found that the Hartmann number, the ratio of magnetic force to viscous force, had a more pronounced impact on non-Newtonian third-grade suspensions than Newtonian fluids. Das et al. [8] discussed the aspects of Arrhenius dynamics and Hall current on an accelerating Couette flow with nanoparticles. The study shows that thermal profile and heat transfer rate manifest a diminishing pattern over widening Hall and rotation parameters. The change in thermal conductivity has a substantial impact on heat transmission. Several studies have presented significant findings regarding flow in a channel medium. The following research studies have contributed to understanding the behaviour of fluids under various conditions in a channel flow problem, including the effects of different fluid properties, external forces, and boundary conditions. Each study highlights specific factors such as fluid type (Newtonian or non-Newtonian), flow configuration (steady or unsteady), and influences like magnetic fields, heat transfer, chemical reactions, or thermal criticality [8–13].

Non-Newtonian fluids have become increasingly prevalent in various industries due to their extensive applications across numerous industrial sectors. Non-Newtonian fluid models such as the Casson, Williamson, and Powell-Erying models have gained significant attention in research because they effectively model the behaviour of many real-world liquids. For instance, blood flow in the human body can be mathematically represented using the Casson fluid model [14, 15], and the Powell-Eyring fluid model can be used to model the behaviour of polymer solutions, biological fluids such as synovial fluid and coating materials [16, 17]. Similarly, the Williamson fluid model can mathematically describe the dynamics of melted plastics and pulp suspensions. This model is especially useful for fluids that exhibit a substantial shear-thinning property, where the viscosity decreases significantly with increased shear stress [9]. The Williamson model captures this behaviour more effectively than the simpler Newtonian model. Patil and Goudar [18] investigated entropy generation and the influence of impulsive acceleration on the Eyring-Powell fluid in a rotating spherical medium with convective assistive flow. The study explored how the Eyring-Powell fluid responds to magnetic effect and irreversibility in the heat transfer. The study's

results suggest that rotational effects significantly impede the fluid flow, leading to a decrease in the fluid velocity as the rotational speed increases. Kudenatti and Noor-E-Misbah [19] analyzed the stability of the hydromagnetic flow of a Casson fluid. The study reveals the emergence of instability in the region close to the wall for specific values of the Casson fluid and the magnetic force parameters. In this region, the associated eigenfunction used to analyze the stability is anti-symmetric with respect to the channel's centre line. Qushairi et al. [20] used the closed-form solution of the mathematical model to examine the parametric influence of various thermophysical properties on the flow of a Casson fluid in a vertically oriented channel.

The viscous and Joule dissipations effect, as well as the influence of magnetohydrodynamics (MHD) on the flow of a Williamson fluid in a microchannel, was studied by Shashikumar et al. [21]. The authors performed an entropy generation analysis, noting that the magnetic field property tends to increase the Bejan number. The study also reported that viscous dissipation leads to an increase in the fluid's temperature distribution. Further insights into the dynamics of the Casson, Powell-Eyring, and Williamson fluids in microchannels can be found in Shashikumar et al. [22] and some of the references therein. In other related studies, Reddy et al. [23] used the machine learning method to analyze the impact of Coriolis force on the flow of dusty micropolar fluid with the addition of nanoparticles over a stretching sheet. The result reveals that dusty hybrid nanofluids exhibit a greater influence than dusty fluids, and enhancing the vortex viscosity and fluid-particle interaction parameters increases the heat transfer rate. Das et al. [24] probed the impact of magnetic field on a dusty Casson fluid due to ramped movement of a thermally active plate. Ali et al. [25] used the neural network to analyze the physical quantities derived in the modelling of MHD tri-hybrid nanofluid streaming inside slanted rotating micro-parallel plates subject to Hall currents.

Entropy generation, as a critical concept in thermodynamics, quantifies the irreversibility of a thermal process [26]. Understanding entropy generation is essential for optimizing thermal management and enhancing efficiency in microfluidic systems. The flow characteristics of fluids, particularly non-Newtonian fluids like Casson, Powell-Eyring, and Williamson, can significantly influence the irreversibility rate, affecting the overall performance of microchannel flow. Entropy generation in microchannel flow can arise from the following sources: viscous dissipation, heat transfer, and energy loss due to magnetic force [21]. As a fluid flows through a microchannel, the shear stress experienced by the fluid particles due to viscosity leads to energy loss in the form of heat, contributing to entropy generation. In non-Newtonian fluids, the nonlinear relationship between shear stress and shear rate complicates the analysis of viscous dissipation [27]. For example, in Casson fluids, the yield stress must be exceeded for significant flow to occur, influencing energy losses and the resulting entropy production.

When fluid flows through a channel, temperature gradients can exist due to external heating or cooling. Heat transfer between the fluid and the channel walls results in entropy generation, particularly if the heat transfer is not uniform. This effect is more pronounced in non-Newtonian fluids, where the thermal properties can differ from those of Newtonian fluids. For example, the temperature distribution in Williamson fluids can vary significantly due to their shear-thinning behaviour, impacting the overall entropy production in the system. Ogunseye et al. [28] investigated the thermal management mechanism in an Eyring-Powell nanofluids flow over a stretching plate. The results indicate that reducing the nanoparticle volume fraction and the Eckert number, a parameter which characterizes the flow's thermal dissipation, decreased the entropy generation within the system. Jakeer et al. [29] studied the degree of randomness in bio-hybrid nanofluid using Fe_3O_4-CuO as a catalyst for blood flow through an induced magnetic field on an expanding surface.

Many deterministic models in fluid dynamics often lack closed-form or analytical solutions. Developing techniques or methods to solve these equations is crucial for facilitating their physical interpretation. Several approaches have been employed for this purpose, including semi-analytical techniques [30, 31], numerical methods [32], and increasingly popular are neural networks-based methods [33–35]. Each of these methodologies offers unique advantages and provides insights into the complex behaviours of fluid systems that are difficult to capture using analytical methods alone. In this study, we employ the Adomian decomposition method and a deep learning approach to analyze the dynamics of the proposed model. The Adomian decomposition method (ADM) is a semi-analytical approach to solving differential equations, particularly useful for nonlinear problems [36]. This method involves decomposing the solution into a series of functions, allowing for the systematic construction of an approximate solution. One of the main advantages of ADM is its ability to handle complex non-linearities without the need for linearization, which is often required in some numerical methods [37]. Deep learning techniques have emerged as powerful tools for solving deterministic models, especially in cases where traditional numerical methods may struggle. Deep learning (DL) algorithms can learn the underlying physics of a problem and its associated conditions, enabling them to approximate solutions to complex differen-

tial equations. A key advantage of DL is its ability to handle high-dimensional spaces and capture nonlinear relationships effectively.

The uniqueness of this study lies in its simultaneous analysis of the flow and thermal behaviour of three non-Newtonian fluids, the investigation of the flow dynamics of a hybrid ferrofluid infused with nanoparticles, and the application of both the Adomian and deep learning methods. Additionally, it explores entropy generation in the heat transfer process. To the best of the authors' knowledge, no study has yet reported the dynamical simulation of three complex fluids in a microchannel with ferro-particles as additives while also analyzing irreversibility in the system.

Mathematical formulation

This study considers the steady, fully developed incompressible flow of a combined non-Newtonian fluid model, specifically the Casson, Williamson, and Powell-Eyring hybrid nanofluid (CWPEHF), within a microchannel. The hybrid nanofluid is presumed to be in thermal equilibrium and adheres to no-slip boundary conditions. The microchannel is characterized by two parallel horizontal plates separated by a distance, h, with the lower plate at $y = 0$ and the upper plate at $y = h$ (see Fig. 1). The flow is based on the following assumptions:

- An external transverse and uniform magnetic field of strength B_0 is applied parallel to the flow direction,
- The flow is subjected to viscous dissipation and Joule heating,
- And the magnetic Reynolds number and induced electric field effects are negligible.

Under the assumptions mentioned above, the momentum and heat balance equations for the CWPEHF are given as follows (see Shashikumar et al. [21, 22], Ogunseye and Sibanda [38]):

$$\rho_{hnf} V_0 \frac{du}{dy} = -\frac{dP}{dx} + \left(\mu_{hnf}\left(1+\frac{1}{\beta}\right)+\frac{1}{bc}\right)\frac{d^2u}{dy^2} + \left(\frac{\mu_{hnf}\Gamma}{\sqrt{2}}\left(\frac{du}{dy}\right) - \frac{1}{2bc^3}\left(\frac{du}{dy}\right)^2\right)\frac{d^2u}{dy^2} - \sigma_{hnf} B_0^2 u, \tag{1}$$

$$(\rho C_p)_{hnf} V_0 \frac{dT}{dy} = k_{hnf}\frac{d^2T}{dy^2} + \left(\mu_{hnf}\left(1+\frac{1}{\beta}\right) + \frac{1}{bc}\right)\left(\frac{du}{dy}\right)^2 + \left(\frac{\mu_{hnf}\Gamma}{\sqrt{2}}\left(\frac{du}{dy}\right) - \frac{1}{6bc^3}\left(\frac{du}{dy}\right)^2\right)\left(\frac{du}{dy}\right)^2 + \sigma_{hnf} B_0^2 u^2, \tag{2}$$

where the subscript hnf denotes the hybrid nanofluid, β is the Casson parameter, ρ_{hnf} is the density, V_0 is the uniform suction/injection velocity at the channel plates, u is the axial velocity, μ_{hnf} is the dynamic viscosity, b and c are fluid constants, Γ is Williamson fluid parameter, σ_{hnf} is the electrical conductivity, T is the temperature, T_0 is the ambient temperature, $(C_p)_{hnf}$ is the heat capacitance, and k_{hnf} is thermal conductivity. The relevant boundary conditions are

$$u = 0, \quad T = T_0, \quad \text{at} \quad y = 0, \tag{3}$$

$$u = 0, \quad T = T_h, \quad \text{at} \quad y = h. \tag{4}$$

In this study, we use the hybrid alumina-ferrofluids (HAF), which is synthesized by adding Fe_2O_3 (25 wt%) and Al_2O_3 (75 wt%) into deionized water as a base fluid using the two-step method [39]. The following empirical relations of

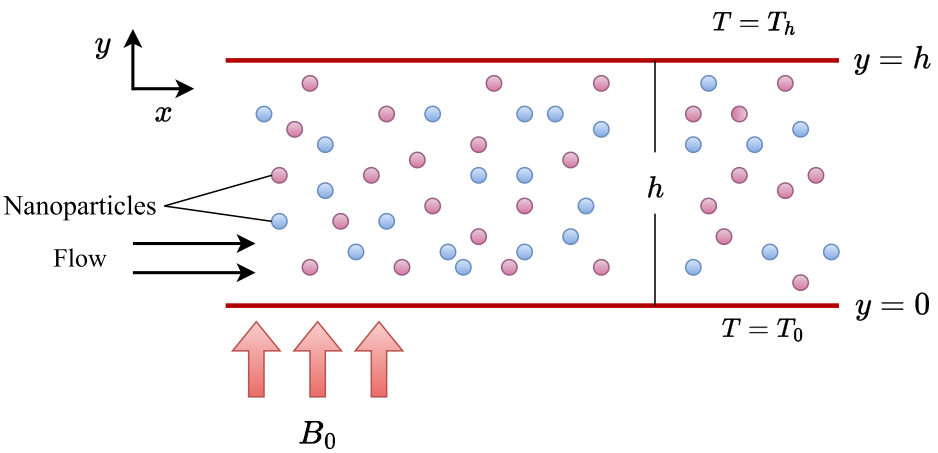


Fig. 1 Geometrical configuration of the microchannel flow of the hybrid alumina ferrofluid

the dynamic viscosity, density, electrical conductivity, thermal conductivity, and specific heat capacity of the HAF are defined as follows:

$$\left.\begin{aligned}
\frac{\mu_{hnf}}{\mu_f} &= \frac{1}{\left(1-\varphi_{Fe_2O_3}\right)^{2.5}\left(1-\varphi_{Al_2O_3}\right)^{2.5}},\\
\frac{\rho_{hnf}}{\rho_f} &= \left(1-\varphi_{Al_2O_3}\right)\left(1-\varphi_{Fe_2O_3}+\varphi_{Fe_2O_3}\frac{\rho_{Fe_2O_3}}{\rho_f}\right)+\varphi_{Al_2O_3}\frac{\rho_{Al_2O_3}}{\rho_f},\\
\frac{(\rho C_p)_{hnf}}{(\rho C_p)_f} &= \left(1-\varphi_{Al_2O_3}\right)\left(1-\varphi_{Fe_2O_3}+\varphi_{Fe_2O_3}\frac{(\rho C_p)_{Fe_2O_3}}{(\rho C_p)_f}\right)+\varphi_{Al_2O_3}\frac{(\rho C_p)_{Al_2O_3}}{(\rho C_p)_f},\\
\frac{\sigma_{hnf}}{\sigma_{bf}} &= \frac{\sigma_{Al_2O_3}+2\sigma_{bf}-2\varphi_{Al_2O_3}\left(\sigma_f-\sigma_{Al_2O_3}\right)}{\sigma_{Al_2O_3}+2\sigma_{bf}+\varphi_{Al_2O_3}\left(\sigma_f-\sigma_{Al_2O_3}\right)},\\
\text{where}\quad \frac{\sigma_{bf}}{\sigma_f} &= \frac{\sigma_{Fe_2O_3}+2\sigma_f-2\varphi_{Fe_2O_3}\left(\sigma_f-\sigma_{Fe_2O_3}\right)}{\sigma_{Fe_2O_3}+2\sigma_f+\varphi_{Fe_2O_3}\left(\sigma_f-\sigma_{Fe_2O_3}\right)},\\
\frac{k_{hnf}}{k_{bf}} &= \frac{k_{Al_2O_3}+2k_{bf}-2\varphi_{Al_2O_3}\left(k_f-k_{Al_2O_3}\right)}{k_{Al_2O_3}+2k_{bf}+\varphi_{Al_2O_3}\left(k_f-k_{Al_2O_3}\right)},\\
\text{where}\quad \frac{k_{bf}}{k_f} &= \frac{k_{Fe_2O_3}+2k_f-2\varphi_{Fe_2O_3}\left(k_f-k_{Fe_2O_3}\right)}{k_{Fe_2O_3}+2k_f+\varphi_{Fe_2O_3}\left(k_f-k_{Fe_2O_3}\right)}.
\end{aligned}\right\} \tag{5}$$

The thermophysical properties of water and the hybrid nanoparticles are given in Table 1.

We define the following dimensionless variables to express Eqs. 1 to 4 in a non-dimensional form [22]:

$$\eta=\frac{y}{h},\quad f(\eta)=\frac{uh\rho_f}{\mu_f},\quad \theta(\eta)=\frac{T-T_0}{T_h-T_0}. \tag{6}$$

Using Eq. 6, Eqs. 1 to 4 become the following dimensionless form:

$$\left(\alpha_1\left(1+\frac{1}{\beta}+Wef'\right)+\lambda_1\right)f''-\lambda_1\lambda_2\left(f'\right)^2f''-\alpha_2Ref'-\alpha_3Ha^2f+P=0, \tag{7}$$

$$\alpha_4\theta''-\alpha_5Pe\theta'+Br\left[\left(\alpha_1\left(1+\frac{1}{\beta}+Wef'\right)+\lambda_1-\frac{1}{3}\lambda_1\lambda_2\left(f'\right)^2\right)\left(f'\right)^2+\alpha_3Ha^2f^2\right]=0, \tag{8}$$

$$f=0,\quad \theta=0,\quad \text{at}\quad \eta=0, \tag{9}$$

$$f=0,\quad \theta=1,\quad \text{at}\quad \eta=1, \tag{10}$$

where $\alpha_1=\frac{\mu_{hnf}}{\mu_f}$, $\alpha_2=\frac{\rho_{hnf}}{\rho_f}$, $\alpha_3=\frac{\sigma_{hnf}}{\sigma_f}$, $\alpha_4=\frac{k_{hnf}}{k_f}$, $\alpha_5=\frac{(\rho C_p)_{hnf}}{(\rho C_p)_f}$, $We=\frac{\mu_f\Gamma}{h^2\rho_f\sqrt{2}}$ is dimensionless Weissenberg number, $\lambda_1=\frac{1}{\mu_f bc}$ and $\lambda_2=\frac{\mu_f^2}{2c^2h^4\rho_f^2}$ are Eyring-Powell fluid parameters, $Re=\frac{\rho_fV_0h}{\mu_f}$ is the Reynolds number, $Ha=B_0h\sqrt{\frac{\sigma_f}{\mu_f}}$ is the Hartmann number, $P=\frac{\rho_fh^3}{\mu_f^2}\left(-\frac{dP}{dx}\right)$ is the axial pressure gradient parameter, $Pe=RePr=\frac{V_0h\left(\rho C_p\right)_f}{k_f}$, is Péclét number, $Pr=\frac{\mu_f\left(C_p\right)_f}{k_f}$ is the Prandtl number, $Br=PrEc=\frac{\mu_f^3}{\rho_f^2k_fh^2\left(T_h-T_0\right)}$ is the Brinkman number and $Ec=\frac{\mu_f^2}{\rho_f^2\left(C_p\right)_fh^2\left(T_h-T_0\right)}$ is the Eckert number.

It is worth mentioning that from Eqs. 7 and 8, we have the following cases of the non-Newtonian hybrid nanofluid:

1. If $We=\lambda_1=0$, and $\beta\in\mathbb{R}^+\backslash\{0\}$, then the model represents the case of the flow of the Casson hybrid nanofluid.
2. If $We=0,\lambda_1\neq0$ and $\beta\longrightarrow\infty$, then the problem reduces to the case of the flow of the hybrid Eyring-Powell nanofluid.
3. If $\beta\longrightarrow\infty$ and $\lambda_1=0$, $We\neq0$, then the Williamson hybrid nanofluid flow case is recovered.

The physical property of interest is the local Nusselt number Nu, which according to López et al. [42] is defined as follows:

$$Nu=-\frac{hk_{hnf}}{2k_f\left(T(y=0)-T_b\right)}\left.\frac{dT}{dy}\right|_{y=0}, \tag{11}$$

Table 1 Thermo-physical properties of water and hybrid nanoparticles around 25°C

	ρ kg/m^3	C_p J/kgK	k W/mK	σ S/m
Water	997.1	4179	0.613	0.05
Fe_2O_3	5180	670	9.7	0.74×10^{6}
Al_2O_3	3970	765	40	1×10^{-10}

(Source: Aly and Pop [40] and Kumar et al. [41])

where T_b and $T(y=0)$, respectively, are the dimensional expressions of the bulk and plate temperatures at $y=0$. The expression of the bulk temperature, T_b, can be written as

$$T_b = \frac{\int_0^h uTdy}{\int_0^h udy}. \tag{12}$$

Using Eqs. 6 and 12, the dimensionless form of Eq. 11 is given as

$$Nu = \frac{\alpha_4}{2\left(\frac{\int_0^1 f\theta d\eta}{\int_0^1 fd\eta}\right)} \left.\frac{d\theta}{d\eta}\right|_{\eta=0}. \tag{13}$$

Entropy generation

Efficient energy management is essential in many thermodynamic processes, mainly when heat loss is substantial. It is, therefore, crucial to examine the system's entropy generation. According to Bejan [43], the rate of local entropy formation per unit volume in the nanofluid flow within the channel is defined as the sum of all terms contributing to entropy generation in the flow. The local entropy generation rate for the microchannel flow currently under study is defined as

$$S_G = \underbrace{\frac{k_{hnf}}{T_0^2}\left(\frac{dT}{dy}\right)^2}_{\text{First term}} + \underbrace{\frac{1}{T_0}\left[\left(\mu_{hnf}\left(1+\frac{1}{\beta}\right)+\frac{1}{bc}\right)\left(\frac{d\bar{u}}{dy}\right)^2 + \frac{\mu_{hnf}\Gamma}{\sqrt{2}}\left(\frac{du}{dy}\right)^3 - \frac{1}{6bc^3}\left(\frac{du}{dy}\right)^4\right]}_{\text{Second term}} + \underbrace{\frac{\sigma_{hnf}B_0^2}{T_0}u^2}_{\text{Third term}}. \tag{14}$$

In Eq. 14, the first term represents heat entropy generation due to heat transfer, the second term denotes entropy production due to fluid frictional interaction, and the third term represents entropy generation due to magnetic flow. Using Eq. 6, we define the total entropy generation in the flow, which is the ratio of the local entropy generation in the microchannel flow and the characteristics rate of entropy generation, in dimensionless form as

$$Ns = \frac{T_0h^2S_G}{k_f\left(T_h-T_0\right)^2} = \alpha_4\left(\theta'\right)^2 + \frac{Br}{\Omega}\left[\left(\alpha_1\left(1+\frac{1}{\beta}+Wef'\right)+\lambda_1-\frac{1}{3}\lambda_1\lambda_2\left(f'\right)^2\right)\left(f'\right)^2+\alpha_3Ha^2f^2\right], \tag{15}$$

where Ω is the temperature difference. The Bejan number determines the relative effects of the heat transfer irreversibility and irreversibility due to the combined effects of viscous dissipation and magnetic field in the entropy generation. Hence, the expression for the Bejan number, Be, is given by [43]

$$Be = \frac{N_h}{N_h+N_f} = \frac{1}{1+M}, \tag{16}$$

where

$$N_h = \alpha_5\left(\theta'\right)^2, \quad N_f = \frac{Br}{\Omega}\left[\left(\alpha_1\left(1+\frac{1}{\beta}+Wef'\right)+\lambda_1-\frac{1}{3}\lambda_1\lambda_2\left(f'\right)^2\right)\left(f'\right)^2+\alpha_3Ha^2f^2\right]. \tag{17}$$

Here, N_h denotes the heat transfer irreversibility, N_f is the irreversibility due to the combined effects of viscous dissipation and magnetic field, and $M = N_f/N_h$ is the irreversibility ratio.

Deep neural networks approximation of the model solution

In this section, we implemented the classical deep neural networks (DNN) framework following the description of Raissi et al. [44] to find the approximate solution of the boundary value problem described by Eqs. 7 to 10. The solutions, $f(\eta)$ and $\theta(\eta)$, are approximated by fully connected feed-forward deep neural networks. The deep neural networks framework takes the independent variable, $\boldsymbol{\eta}$, as input and produces the approximate solution, $[\mathbf{f}_{NN}(\boldsymbol{\eta}), \theta_{NN}(\boldsymbol{\eta})]$, of the model as outputs. Consider the deep neural network architecture composed of $n+1$ layers, beginning with an input layer and ending with an output layer, as in Fig. 2. The input layer, denoted by $y_0 = \boldsymbol{\eta}$, represents the initial input vector fed into the network. This input is then sequentially propagated through the hidden layers, where each hidden layer's output y_j is computed as

$$y_j = \phi(w_j y_{j-1} + b_j), \quad j = 1, \ldots, n-1, \tag{18}$$

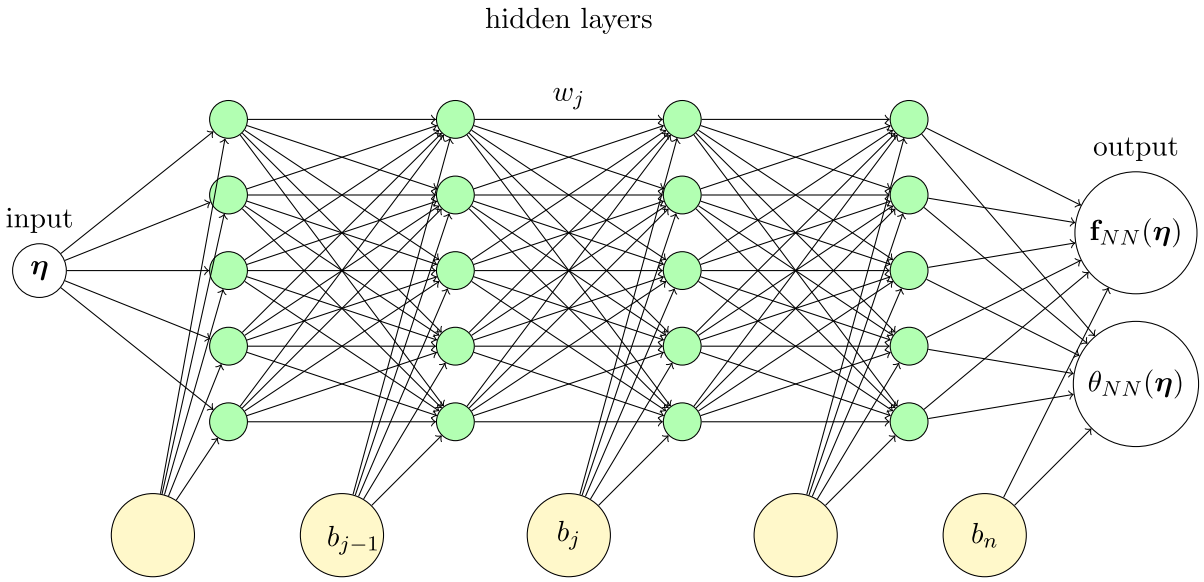


Fig. 2 Schematic diagram of a fully connected deep neural network architecture

where $\phi(\cdot)$ is the nonlinear sigmoidal activation function applied element-wise, w_j represents the trainable weight matrix, and b_j denotes the trainable bias vector at layer j. Finally, in the output layer, the network produces y_n by applying a linear transformation as

$$y_n = w_n y_{n-1} + b_n = [\mathbf{f}_{NN}(\boldsymbol{\eta}), \theta_{NN}(\boldsymbol{\eta})], \tag{19}$$

where $\mathbf{f}_{NN}(\boldsymbol{\eta})$ and $\theta_{NN}(\boldsymbol{\eta})$ are the network's outputs, representing distinct functions of the input vector $\boldsymbol{\eta}$ tailored to the microchannel flow problem at hand. The parameters of the network, namely the weights and biases, are trained by minimizing the composite loss function presented in the form

$$\mathcal{L}(\boldsymbol{\eta}; w, b) = \mathcal{L}_\eta + \mathcal{L}_0 + \mathcal{L}_h, \tag{20}$$

where

$$\mathcal{L}_\eta = \frac{1}{N_\eta}\sum_{i=1}^{N_\eta}\left[\left|N_f[\mathbf{f}_{NN}(\boldsymbol{\eta}_i)]\right|^2 + \left|N_\theta[\mathbf{f}_{NN}(\boldsymbol{\eta}_i), \theta_{NN}(\boldsymbol{\eta}_i)]\right|^2\right], \tag{21a}$$

$$\mathcal{L}_0 = \left|\mathbf{f}_{NN}(\boldsymbol{\eta}_1)\right|^2 + \left|\theta_{NN}(\boldsymbol{\eta}_1)\right|^2, \tag{21b}$$

$$\mathcal{L}_h = \left|\mathbf{f}_{NN}(\boldsymbol{\eta}_{N_\eta})\right|^2 + \left|\theta_{NN}(\boldsymbol{\eta}_{N_\eta}) - 1\right|^2. \tag{21c}$$

Here, $\mathcal{L}_\eta$ penalizes the residuals of the equations, and $\mathcal{L}_0$ and $\mathcal{L}_h$ penalize the residuals of the boundary conditions; N_η represents the number of input data points; N_f and N_θ are the nonlinear differential operator defined as

$$N_f[f(\eta)] = \left(\alpha_1\left(1+\frac{1}{\beta}+Wef'\right)+\lambda_1\right)f'' - \lambda_1\lambda_2\left(f'\right)^2 f'' - \alpha_2 Ref' - \alpha_3 Ha^2 f + P, \tag{22}$$

$$N_\theta[f(\eta), \theta(\eta)] = \alpha_4\theta'' - \alpha_5 Pe\theta' + Br\left[\left(\alpha_1\left(1+\frac{1}{\beta}+Wef'\right)+\lambda_1-\frac{1}{3}\lambda_1\lambda_2\left(f'\right)^2\right)\left(f'\right)^2 + \alpha_3 Ha^2 f^2\right]. \tag{23}$$

The weights and biases in each hidden layer are updated by solving the unconstrained optimization problem, that is, minimizing the loss function (20), using the limited-memory Broyden–Fletcher–Goldfarb–Shanno (L-BFGS) algorithm. The L–BFGS algorithm is a quasi-Newton method that approximates the inverse of the Hessian matrix, the second-order derivative of the loss function, to efficiently guide the search of the neural network model parameters. Unlike the conventional BFGS algorithm, the L-BFGS uses a limited memory representation, making it particularly feasible for the optimization of large-scale problems [45]. Suppose the weights and biases of the neural network framework are defined together as a parameter vector $\mathcal{V} = [w_1, b_1, \ldots, w_{j-1}, b_{j-1}, w_j, b_j, \ldots, w_n, b_n]^\mathsf{T}$, then the update rule for the parameter vector is given by

$$\mathcal{V}^{k+1} = \mathcal{V}^k - \alpha^k \mathcal{H}^k \nabla\mathcal{L}(\boldsymbol{\eta}; \mathcal{V}^k), \tag{24}$$

where $\mathcal{V}^k$ is the parameter vector at the k-th iteration, α^k is the step-size at the k-iteration obtained through line search, $\mathcal{H}$ is the approximation of the inverse Hessian matrix, and $\nabla\mathcal{L}(\boldsymbol{\eta};\mathcal{V})$ is the gradient vector of the loss function (20), which is the partial derivatives of the loss function $\mathcal{L}(\boldsymbol{\eta};w,b)$ with respect to the weights and biases,

$$\nabla\mathcal{L}(\boldsymbol{\eta};w,b)=\left[\frac{\partial\mathcal{L}}{\partial w_1},\frac{\partial\mathcal{L}}{\partial b_1},\ldots,\frac{\partial\mathcal{L}}{\partial w_{j-1}},\frac{\partial\mathcal{L}}{\partial b_{j-1}},\frac{\partial\mathcal{L}}{\partial w_j},\frac{\partial\mathcal{L}}{\partial b_j},\ldots,\frac{\partial\mathcal{L}}{\partial w_n},\frac{\partial\mathcal{L}}{\partial b_n}\right]^{\mathsf{T}},\tag{25}$$

computed using backpropagation. Instead of using the full Hessian matrix, the L-BFGS algorithm maintains a history of m gradient updates $(\nabla\mathcal{L}(\boldsymbol{\eta};\mathcal{V}^{i+1})-\nabla\mathcal{L}(\boldsymbol{\eta};\mathcal{V}^{i}))$ and parameter differences $(\mathcal{V}^{i+1}-\mathcal{V}^{i})$ to construct a low-rank approximation of the inverse Hessian. The update for $\mathcal{H}^k$ is calculated using the following recursive formula:

$$\mathcal{H}^{k+1}=(\mathcal{B}^k)^{\mathsf{T}}\mathcal{H}^k\mathcal{B}^k+\mathcal{A}^k(\mathcal{V}^{k+1}-\mathcal{V}^k)(\mathcal{V}^{k+1}-\mathcal{V}^k)^{\mathsf{T}},\tag{26}$$

where

$$\mathcal{A}^k=\frac{1}{(\nabla\mathcal{L}(\boldsymbol{\eta};\mathcal{V}^{k+1})-\nabla\mathcal{L}(\boldsymbol{\eta};\mathcal{V}^k))^{\mathsf{T}}(\mathcal{V}^{k+1}-\mathcal{V}^k)},\tag{27}$$

$$\mathcal{B}^k=\mathcal{I}-\mathcal{A}^k(\nabla\mathcal{L}(\boldsymbol{\eta};\mathcal{V}^{k+1})-\nabla\mathcal{L}(\boldsymbol{\eta};\mathcal{V}^k))(\mathcal{V}^{k+1}-\mathcal{V}^k)^{\mathsf{T}},\tag{28}$$

and $\mathcal{H}^0$ is the initial approximation of the inverse Hessian matrix. At each iterative level, a line search is done to determine the optimal step-size α^k so that there is a sufficient decrease in the loss function and α^k satisfies the Wolfe condition:

$$\left.\begin{aligned}&\mathcal{L}(\boldsymbol{\eta};\mathcal{V}^{k+1})\le\mathcal{L}(\boldsymbol{\eta};\mathcal{V}^k)+c_1\alpha^k(\nabla\mathcal{L}(\boldsymbol{\eta};\mathcal{V}^k))^{\mathsf{T}}\mathcal{P}^k,\\&-(\nabla\mathcal{L}(\boldsymbol{\eta};\mathcal{V}^{k+1}))^{\mathsf{T}}\mathcal{P}^k\le-c_2(\nabla\mathcal{L}(\boldsymbol{\eta};\mathcal{V}^k)^{\mathsf{T}}\mathcal{P}^k,\end{aligned}\right\}\tag{29}$$

where $\mathcal{P}^k=-\mathcal{H}^k\nabla\mathcal{L}(\boldsymbol{\eta};\mathcal{V}^k)$ is the search direction and $0<c_1<c_2<1$. The algorithm iteratively updates the weights and biases until a stopping criterion is met or a predefined number of iterations is reached. The deep learning technique described herein is implemented using the Julia programming language [46]. The pseudocode for the algorithm is provided in Algorithm 1.

Algorithm 1 Pseudocode for the deep neural network training with L-BFGS algorithm.

Require: Input vector data $\boldsymbol{\eta}$, initial parameter vector $\mathcal{V}$, loss function $\mathcal{L}(\boldsymbol{\eta};\mathcal{V})$, maximum iterations `max_iters`, tolerance `tol`
Ensure: Optimized parameter vector $\mathcal{V}^*$
Initialize $\mathcal{V}\leftarrow$ `random_init()`, $k\leftarrow 0$
function FORWARDPASS($\boldsymbol{\eta},\mathcal{V}$)
  for each layer $j=1,\ldots,n$ **do**
    Compute pre-activation: $y_j=w_jy_{j-1}+b_j$
    Apply activation: $y_j=\phi(y_j)$
    if $j==n$ **then**
      Compute: $y_n=w_ny_{n-1}+b_n$
    end if
  end for
  return y_n
end function
function LOSSFUNCTION($\mathcal{V}$)
  $[\mathbf{f}_{NN}(\boldsymbol{\eta}),\theta_{NN}(\boldsymbol{\eta})]\leftarrow$ `ForwardPass`$(\boldsymbol{\eta},\mathcal{V})$
  Compute loss: $\mathcal{L}(\boldsymbol{\eta};\mathcal{V})=Eq.20$
  return $\mathcal{L}(\boldsymbol{\eta};\mathcal{V})$
end function
function GRADIENT($\mathcal{V}$)
  Compute $\nabla\mathcal{L}(\boldsymbol{\eta};\mathcal{V})$ using backpropagation
  return $\nabla\mathcal{L}(\boldsymbol{\eta};\mathcal{V})$
end function
function LINESEARCH($\mathcal{V},\mathcal{P}^k$)
  Find step size α^k that satisfies Wolfe conditions Eq. 29
  return α^k
end function
while $k<$ `max_iters` **do**
  Compute current loss: $\mathcal{L}_{\text{current}}=$ `LossFunction`$(\mathcal{V})$
  Compute gradient: `Gradient`$(\mathcal{V})$
  if $\|\mathcal{L}_{\text{current}}\|<$ `tol` **then**
    break
  end if
  Approximate inverse Hessian $\mathcal{H}^k$ using the L-BFGS algorithm
  Compute search direction: $\mathcal{P}^k=-\mathcal{H}^k\nabla\mathcal{L}(\boldsymbol{\eta};\mathcal{V})$
  Perform line search: $\alpha^k=$ `LineSearch`$(\mathcal{V},\mathcal{P}_k)$
  Update parameters: $\mathcal{V}\leftarrow\mathcal{V}-\alpha^k\mathcal{H}^k\nabla\mathcal{L}(\boldsymbol{\eta};\mathcal{V})$
  Increment iteration: $k\leftarrow k+1$
end while
return Optimized parameter vector $\mathcal{V}^*$

Adomian decomposition method for approximating the model solution

This section focuses on applying the Adomian decomposition method (ADM) to solve the nonlinear boundary value problems in Eqs. 7 to 10. Due to the nonlinearity involved, the choice of method is suitable for constructing a semi-analytical solution. The ADM was introduced in Adomian [47] where the method was used to solve nonlinear oscillatory systems in physics, the Duffing equation, boundary value problems with closed irregular contours or surfaces, and other deterministic differential equations. Consider the general equation:

$$\varphi[u(y)]=g(y),\tag{30}$$

where φ represents a general non-linear ordinary (or partial) differential operator involving both linear and non-linear terms. The linear terms are decomposed into the form $L+R$, where L is usually taken as the highest order derivative, which is assumed to be easily invertible, and R is the linear differential operator of order less than L. Therefore, Eq. 30

can be expressed as

$$Lu + Ru + Nu = g(y), \tag{31}$$

where Nu represents the non-linear terms of $\varphi[u]$. Applying the inverse operator, L^{-1}, to both sides of Eq. 31 gives

$$u = L^{-1}g - L^{-1}(Ru + Nu). \tag{32}$$

If L is a fourth-order operator, then L^{-1} is a 4-fold integral. Now, solving Eq. 32, we have

$$u = \sum_{j=0}^{3} \alpha_j \frac{y}{j!} + L^{-1}g - L^{-1}\left(Ru + Nu\right), \tag{33}$$

where $\alpha_j (j = 1..3)$ are constants of integration and can be determined from the given boundary conditions. The standard Adomian decomposition method defines the solution u by the infinite series

$$u = \sum_{n=0}^{\infty} u_n, \tag{34}$$

and the non-linear term by the infinite series

$$Nu = \sum_{n=0}^{\infty} A_n, \tag{35}$$

where A_n are the Adomian polynomials determined formally from the relation;

$$A_n = \frac{1}{n!}\left[\frac{d^n}{d\lambda^n} N\left(\sum_{i=0}^{\infty} \lambda^i u_i\right)\right]_{\lambda=0}, \quad i = 0, 1, 2, \ldots \tag{36}$$

The u_n are determined from the recursive algorithm

$$\begin{aligned} u_0 &= \sum_{j=0}^{3} \alpha_j \frac{y}{j!} + L^{-1}g, \\ u_{n+1} &= -L^{-1}(Ru + Nu) \quad n \geq 0, \end{aligned} \tag{37}$$

where u_0 is the zeroth component. For numerical computation, the truncated series solution is obtained as

$$S_n(y) = \sum_{k=0}^{n-1} u_k, \tag{38}$$

where S_n denotes the $n-$term approximation of $u(y)$.

The solutions of $f(\eta)$ and $\theta(\eta)$ are solved independently since the system of differential equations is loosely coupled. Using the standard methodology for ADM as discussed above (see Wazwaz [36], Duan and Rach [37], Adesanya et al. [48]). Equation 7 can be written in operator form as

$$\begin{aligned} Lf = \frac{1}{\left(\alpha_1\left(1 + \frac{1}{\beta}\right) + \lambda_1\right)}\Big[&\lambda_1\lambda_2\left(f'\right)^2 f'' - \alpha_1 We f' f'' \\ &+ \alpha_2 Re f' + \alpha_3 Ha^2 f - P\Big], \end{aligned} \tag{39}$$

where $L = \frac{d^2}{d\eta^2}$ is a second differential operator, with inverse operator $L^{-1} = \int_0^{\eta}\int_0^{\eta} (\cdot)\, d\tau d\tau$. Applying L^{-1} to both sides of Eq. 39 and imposing the condition $f(0) = 0$ yields

$$\begin{aligned} f = a_1\eta &- \frac{P\eta^2}{2\left(\alpha_1\left(1 + \frac{1}{\beta}\right) + \lambda_1\right)} \\ &+ \frac{1}{\left(\alpha_1\left(1 + \frac{1}{\beta}\right) + \lambda_1\right)} L^{-1}\left[\lambda_1\lambda_2 G_1(f) - \alpha_1 We G_2(f)\right. \\ &\left. + \alpha_2 Re f' + \alpha_3 Ha^2 f\right], \end{aligned} \tag{40}$$

where $a_1 = f'(0)$ is determined by using the boundary condition at $\eta = 1$, and $G_1(f) = \left(f'\right)^2 f''$ and $G_2(f) = f' f''$ are the nonlinear terms. In terms of ADM, $f(\eta)$ is assumed to be a series solution of the form

$$f(\eta) = \sum_{n=0}^{\infty} f_n(\eta), \tag{41}$$

and the nonlinear terms are decomposed as series

$$G_1(f) = \sum_{n=0}^{\infty} A_n, \quad \text{and} \quad G_2(f) = \sum_{n=0}^{\infty} B_n, \tag{42}$$

where A_n and B_n are Adomian's polynomials. The Adomian polynomials are determined from the relation;

$$D_n = \frac{1}{n!}\left[\frac{d^n}{d\lambda^n} N\left(\sum_{i=0}^{\infty} \lambda^i u_i\right)\right]_{\lambda=0}, \quad i = 0, 1, 2, \ldots \tag{43}$$

The first few terms of A_n and B_n are defined below:

$$\begin{aligned} &A_0 = \left(f_0'\right)^2 f_0'', \quad A_1 = \left(f_0'\right)^2 f_1'' + 2 f_0' f_1' f_0'', \\ &A_2 = \left(f_0'\right)^2 f_2'' + 2 f_0' f_1' f_1'' + 2 f_0' f_2' f_0'' + \left(f_1'\right)^2 f_0'', \ldots, \end{aligned}$$

$$B_0 = f_0' f_0'', \quad B_1 = f_0' f_1'' + f_1' f_0'',$$
$$B_2 = f_0' f_2'' + f_1' f_1'' + f_2' f_0'', \ldots.$$

Substituting Eqs. 41 and 42 into Eq. 40 yields

$$\sum_{n=0}^{\infty} f_n(\eta) = a_1\eta - \frac{P\eta^2}{2\left(\alpha_1\left(1+\frac{1}{\beta}\right)+\lambda_1\right)} + \frac{1}{\left(\alpha_1\left(1+\frac{1}{\beta}\right)+\lambda_1\right)} L^{-1}\left[\lambda_1\lambda_2 \sum_{n=0}^{\infty} A_n - \alpha_1 We \sum_{n=0}^{\infty} B_n + \alpha_2 Re \sum_{n=0}^{\infty} f_n' + \alpha_3 Ha^2 \sum_{n=0}^{\infty} f_n\right]. \tag{44}$$

The recursive relations for the semi-analytical solution of Eq. 7, which is obtained from Eq. 44, are given by

$$\left.\begin{aligned} f_0(\eta) &= a_1\eta - \frac{P\eta^2}{2\left(\alpha_1\left(1+\frac{1}{\beta}\right)+\lambda_1\right)} + \frac{1}{\left(\alpha_1\left(1+\frac{1}{\beta}\right)\right)}, \\ f_{n+1}(\eta) &= \frac{1}{\left(\alpha_1\left(1+\frac{1}{\beta}\right)+\lambda_1\right)} L^{-1}\left[\lambda_1\lambda_2 A_n - We B_n + \alpha_2 Re f_n' + \alpha_3 Ha^2 f_n\right], \quad n \geq 0. \end{aligned}\right\} \tag{45}$$

The partial sum

$$f(\eta) = \sum_{k=0}^{n} f_k(\eta). \tag{46}$$

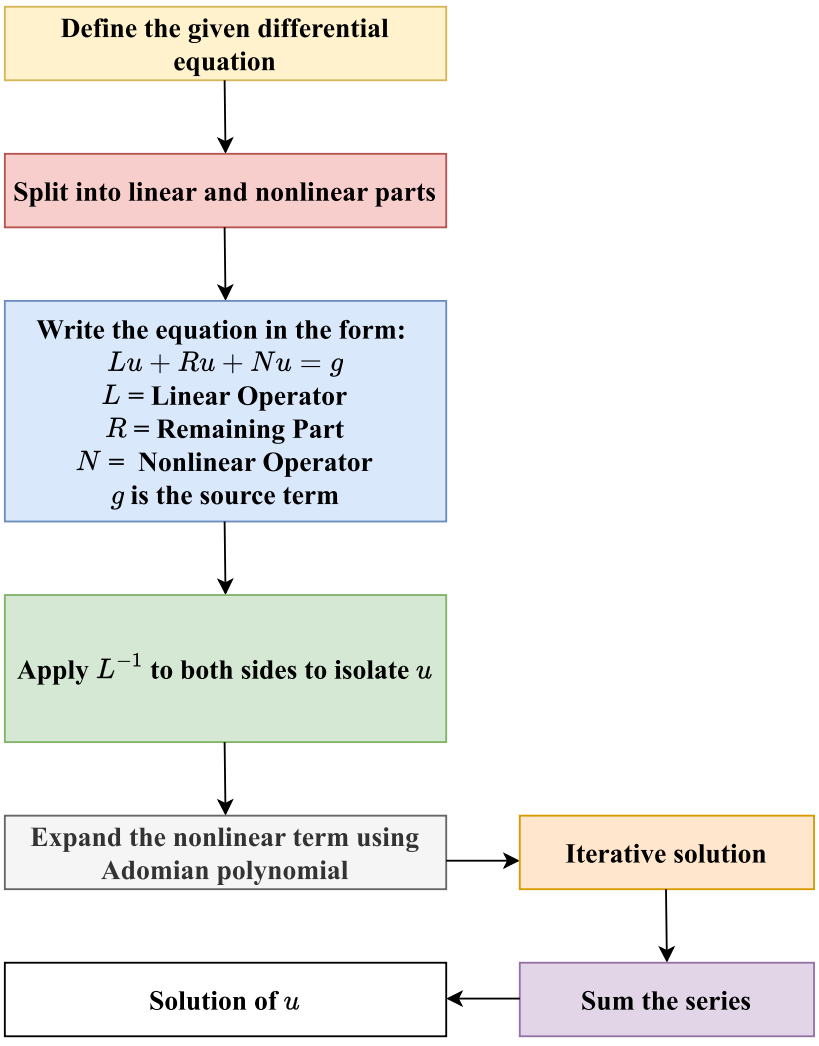


Fig. 3 Flow chart of the Adomian decomposition method

is the approximate solution. In a similar manner, the recursive relation for the semi-analytical solution of Eq. 8 is given as

$$\left.\begin{aligned}\theta_0(\eta) &= a_2 + \frac{\eta\gamma}{\alpha_4}(a_2-1) - \frac{Br}{\alpha_4}L^{-1}\left[\left(\alpha_1\left(1+\frac{1}{\beta}+Wef'\right)+\lambda_1-\frac{1}{3}\lambda_1\lambda_2\left(f'\right)^2\right)\left(f'\right)^2+\alpha_3 Ha^2 f^2\right],\\ \theta_{n+1}(\eta) &= \frac{\alpha_5}{\alpha_4}PeL^{-1}\theta_n', \quad n \geq 0,\end{aligned}\right\} \tag{47}$$

where $a_2 = \theta'(0)$ is determined at using the boundary condition at $\eta = 1$. The partial sum of the approximate solution is given by

$$\theta(\eta) = \sum_{k=0}^{n}\theta_k(\eta). \tag{48}$$

Remark 1 For easy computation of the iterative procedure, the Adomian algorithm is coded on a symbolic Maple-18 package for the evaluation of the tedious integrals. See Fig. 3 for the flow chart of the method.

Results and discussion

In this section, we provide an analysis of the result of the mathematical model presented in Eqs. 7 and 8 with the asso-

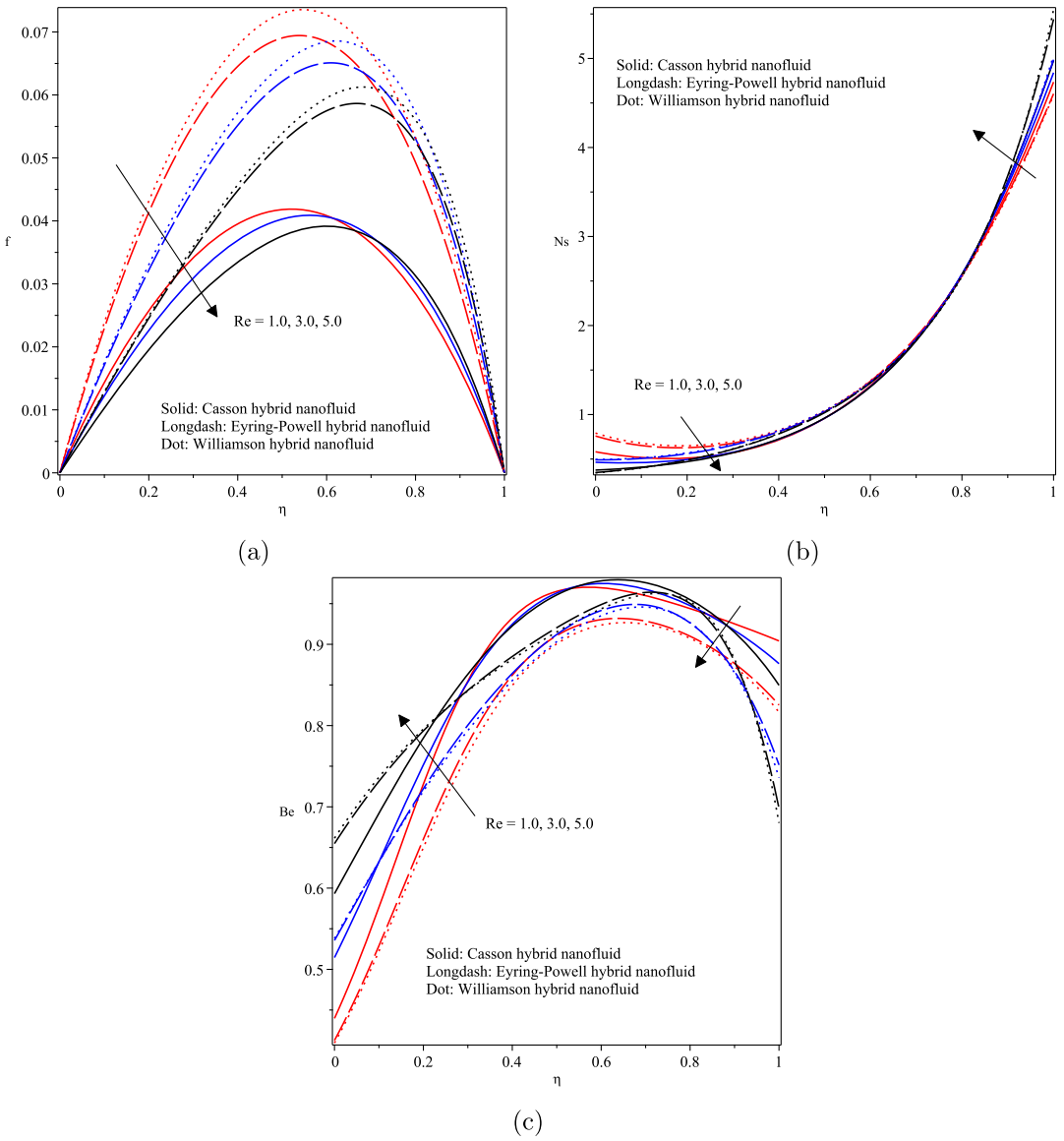


Fig. 4 Effect of varying the Reynolds number *Re* of the hybrid nanofluids: **a** velocity profiles, **b** entropy generation rate, **c** Bejan number

ciated boundary conditions in Eqs. 9 and 10. It is important to highlight that, unless stated otherwise, the default values for the dimensionless parameters used throughout the analysis are as follows: Reynolds number, $Re = 1.0$, Hartmann number $Ha = 2.0$, Weissenberg number, $We = 0.5$, Brinkman number, $Br = 10.0$, Eyring-Powell fluid parameter, $\lambda_2 = 0.5$, pressure gradient constant $P = 1.0$, and Péclét number, $Pe = 2.0$. Where need be, we choose the Casson parameter, $\beta = 1.0$, fluid parameter, $\lambda_1 = 0.1$, and the nanoparticles volume fractions, $\varphi_{Fe_2O_3} = \varphi_{Al_2O_3} = 0.05$. These parameters characterize the behaviour of the system and are essential to understanding the dynamics described by the dynamical model. Figure 4 illustrates the effect of the Reynolds number on the velocity profiles, entropy generation rates, and the Bejan number. The Reynolds number impacts the velocity profile and Bejan number of the hybrid nanofluids. The velocity profile $f(\eta)$ represents the fluid velocity distribution across the channel height (η). The velocity is typically zero at both walls due to the no-slip condition and reaches its maximum around the channel centre. The parabolic profile shows the balance between viscous forces near the walls and inertial forces in the channel core. The Casson fluid (solid line) exhibits the steepest velocity profile, suggesting stronger inertia and higher flow velocities in the channel centre than other fluids. This is due to the lower internal resistance of the Casson hybrid nanofluid, allowing it to respond more rapidly to inertial forces. Eyring-Powell and Williamson fluids (long-dash and dotted lines, respectively) show broader profiles, indicating a more significant influence of viscous forces. These fluids experience greater internal resistance to

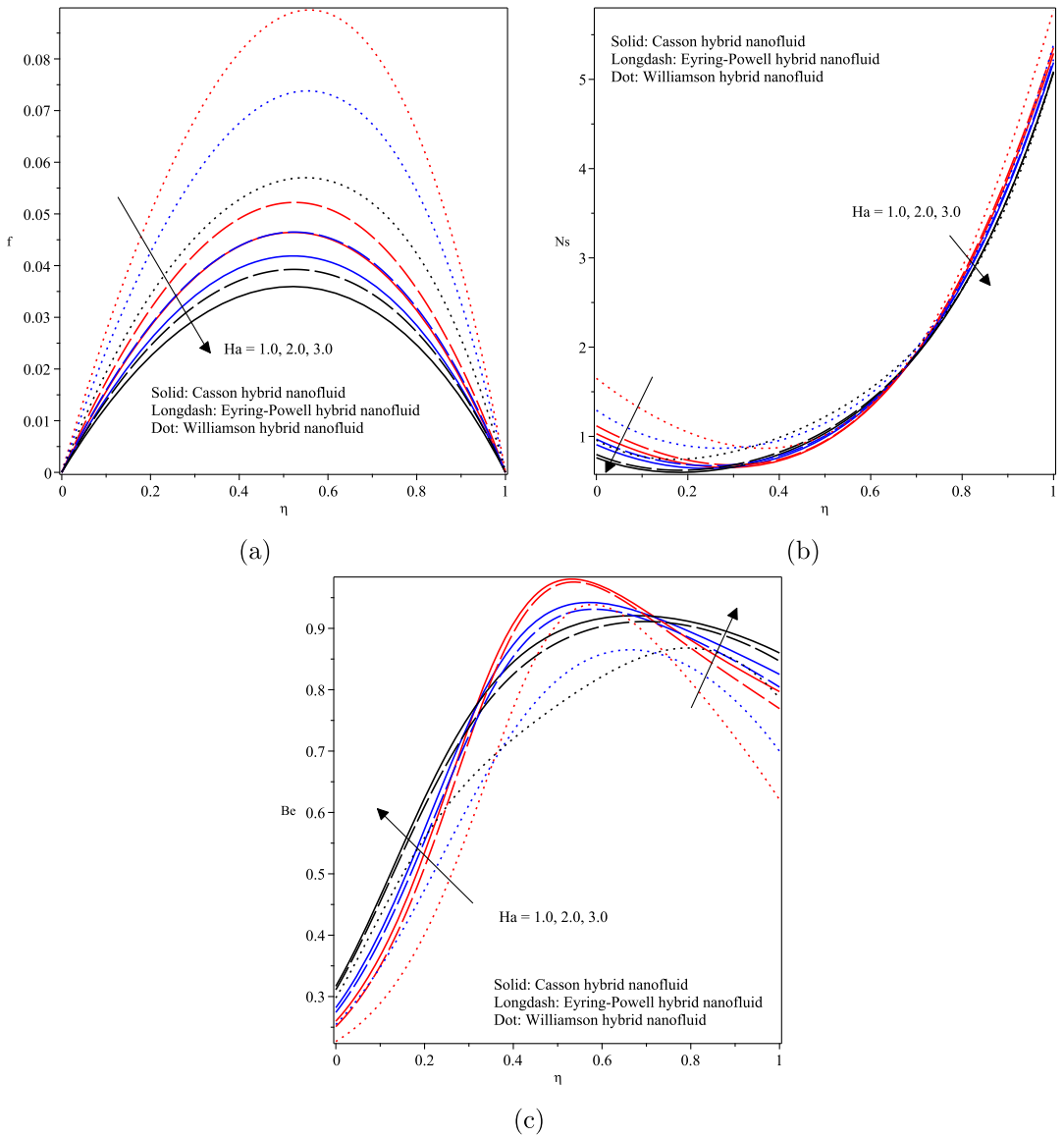


Fig. 5 Effect of increasing the Hartmann number, Ha, on the hybrid nanofluids: **a** velocity profiles, **b** entropy generation rate, **c** Bejan number

deformation, which smoothens the velocity gradient across the channel height. The Bejan number (Be) characterizes the dominance of heat transfer irreversibility over fluid friction irreversibility in the channel. A high Bejan number indicates that heat transfer is the dominant source of entropy generation in the channel region, while a lower Bejan number suggests that frictional losses (due to the fluid's viscosity) are more significant. The Bejan number peaks near the centre of the channel, implying that heat transfer irreversibility is most dominant where the velocity is highest and friction is lower. The Bejan number is lower near the walls, where viscous effects dominate, indicating more entropy generation from fluid friction. The Casson hybrid nanofluid shows a higher Bejan number in the channel's central region than the Eyring-Powell and the Williamson fluids. The Eyring-Powell and the Williamson fluids exhibit lower Bejan numbers across the channel, indicating a greater proportion of entropy generation from fluid friction. This suggests that heat transfer irreversibility is more significant for the Casson fluid, potentially due to better thermal conductivity or reduced frictional losses. Different fluid models (Casson, Eyring-Powell, and Williamson) react differently to changes in Reynolds number, indicating that the choice of the non-Newtonian fluid model plays a significant role in determining the efficiency and irreversibility of the system. Figure 5 shows the effect of the Hartmann number (magnetic parameter) on the fluid's velocity profiles, entropy generation rate, and Bejan number. As the Hartmann number increases, it suppresses the fluid flow, which is consistent with expectations. This is because the Hartmann parameter represents a resistive force that hin-

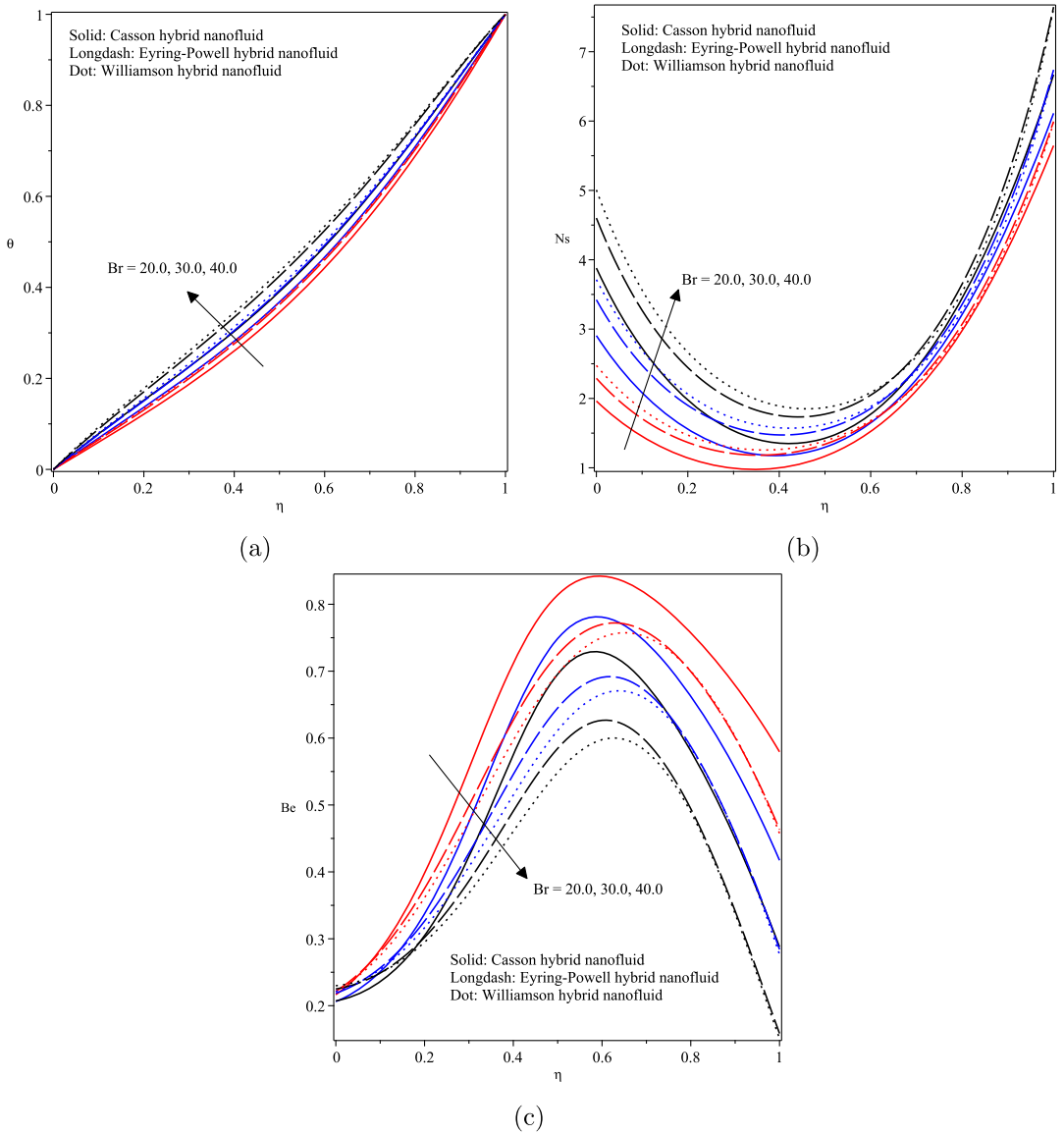


Fig. 6 Effect of varying the Brinkman number, Br, on the hybrid nanofluids: **a** temperature profiles, **b** entropy generation rate, **c** Bejan number

ders the fluid flow within the microchannel. The highest flow rate is observed near the centre of the channel. The entropy generation rate (Ns) quantifies the irreversibility within the system. Higher values indicate greater entropy production, often due to viscous effects, heat transfer, or both. Minimizing entropy generation is desirable for efficient thermal management. The trends show that as Ha increases, there is a general decrease in entropy generation for all the types of fluids, especially near the channel walls ($\eta = 0$) and ($\eta = 1$); the Casson fluid exhibits moderate entropy generation compared to the Eyring-Powell and the Williamson fluids. Increasing the Hartmann number leads to an increase in the Bejan number in the regions close to the lower and upper plates. The Hartmann number represents the influence of the Lorentz force, a resistive electromagnetic force, on fluid motion. This suppression enhances the temperature gradient in regions near the lower and upper plates because the convective heat transfer is reduced, making conductive heat transfer more dominant. Therefore, near the plates, where the temperature gradients are steeper, the Bejan number rises due to the reduced convective flow and enhanced dominance of conduction under a stronger magnetic field.

Figure 6 represents the influence of the Brinkman number (Br) on the system. The Brinkman number is the product of the Prandtl number (Pr) and the Eckert number (Ec). Physically, it characterizes the relationship between viscous dissipation and conductive heat transfer within the fluid. An increase in Br typically signifies that viscous heating effects

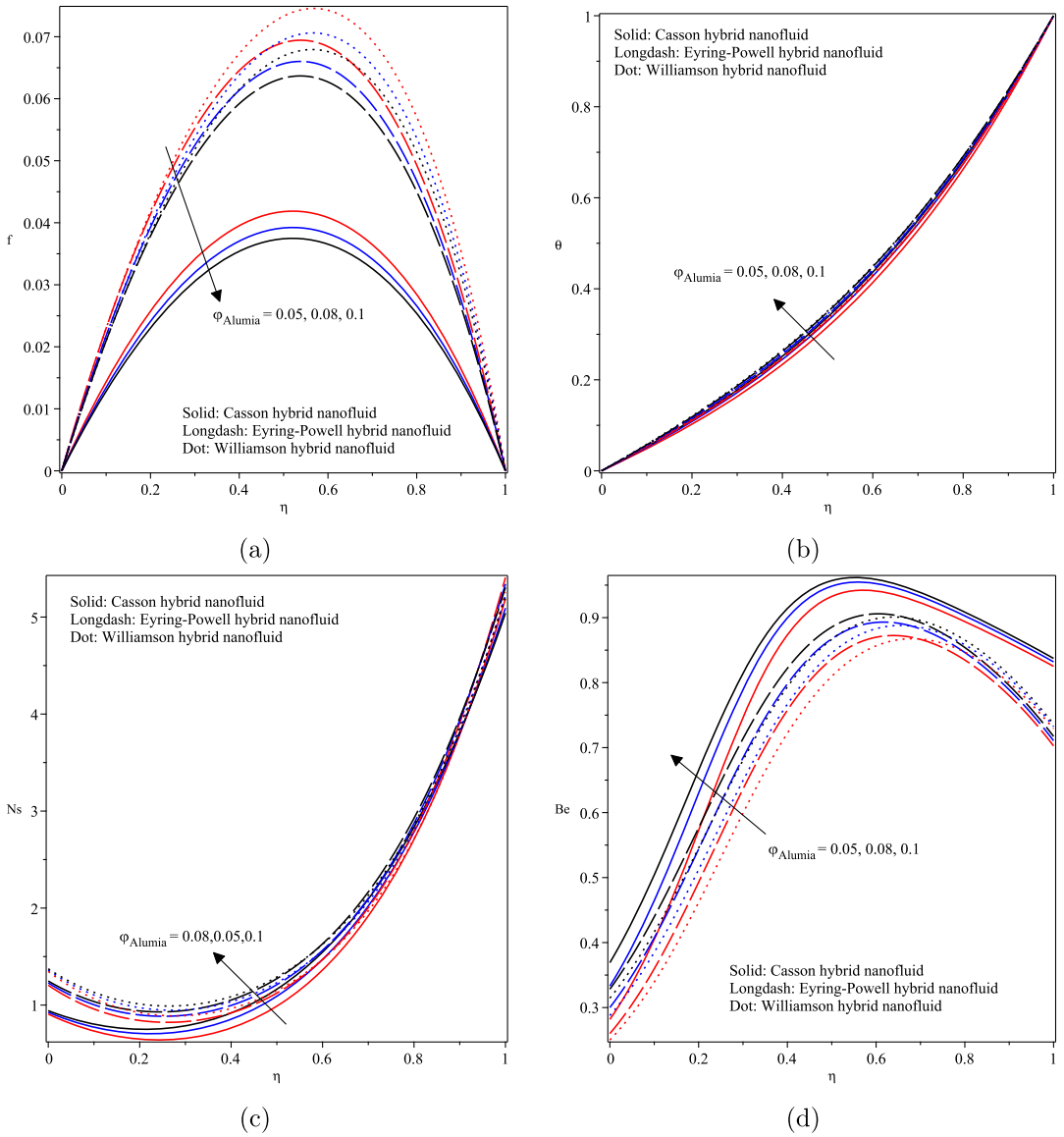


Fig. 7 Effect of varying the nanoparticle volume fraction for Alumia ($\varphi_{Al_2O_3}$) on the hybrid nanofluids: **a** velocity profiles, **b** temperature profiles, **c** entropy generation rate, **d** Bejan number

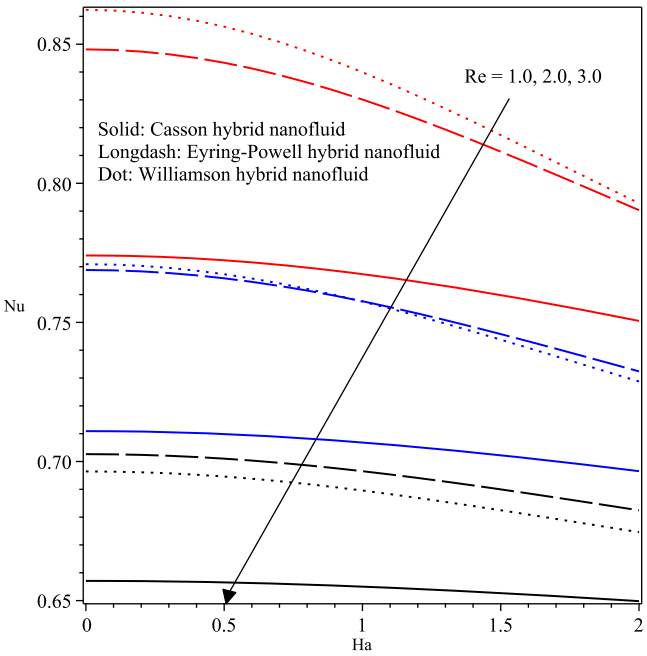


Fig. 8 Effect of Reynolds number on the Nusselt number

become more dominant than heat conduction, leading to notable changes in the fluid's thermal and flow behaviour. A higher Brinkman number indicates slower heat conduction from viscous dissipation, resulting in a greater temperature increase, graphically supported by Fig. 6a. It is observed that the Williamson fluid exhibits the highest thermal sensitivity, while the Casson fluid shows the lowest thermal sensitivity in response to variations in the Brinkman number (Br). In Fig. 6c, as Br increases, the proportion of irreversibility attributed to viscous effects rises. Since Be is the ratio of heat transfer irreversibility to total irreversibility, a higher contribution from viscous dissipation will reduce the fraction that comes from heat transfer. Thus, Be decreases because viscous dissipation dominates the total entropy generation more than thermal effects. Higher Br values suggest better thermal management to offset the effects of increased viscous heating. This might involve improving heat dissipation (e.g., through enhanced heat exchangers or cooling techniques) or reducing viscous effects by altering the fluid's properties (e.g., optimizing flow conditions). When Br increases, the system experiences enhanced viscous dissipation. This means more mechanical energy is being converted into thermal energy through internal friction of the fluid particles, leading to higher entropy production rates, as seen in Fig. 6b. The Casson fluid has the lowest entropy generation rate as we increase the Brinkman parameter, with the Williamson fluid having the highest rate of disorder.

Figure 7 shows the significance of nanoparticle volume fraction in the dynamical system. Increasing the nanoparticle volume fraction reduces the velocity of all the fluids. This is because a higher concentration of nanoparticles causes clogging, which hinders the fluid's ability to flow smoothly. However, this also increases the temperature profile due to increased internal friction between the fluid particles. Figure 7a and b gives the graphical representations of the effect of volume fractions on the velocity and temperature profiles of the fluids. It is observed that adding more nanoparticles to the fluid impedes the flow velocity and increases the temperature of the fluids across the microchannel. The physical implication is that as more nanoparticles are added to the fluid, they clog the fluid flow ability and make it more resistant to motion. However, introducing additional nanoparticles enhances heat transfer within the fluid and its surrounding medium, thereby increasing the temperature profile of the fluid. Increasing the volume fraction for Alu-

Table 2 Comparison of the DNN results for velocity with the ADM and RK4 results for Casson hybrid nanofluid, Eyring-Powell hybrid nanofluids, and Williamson hybrid nanofluid when $Re = P = 1.0$, $Ha = Pe = 2.0$, $Br = 10.0$, and $\varphi_{Fe_2O_3} = \varphi_{Al_2O_3} = 0.05$

	Casson hybrid nanofluid ($\beta = 1.0, We = \lambda_1 = 0$)			Eyring–Powell hybrid nanofluid ($\beta \longrightarrow \infty, We = 0, \lambda_1 = 0.1, \lambda_2 = 1.0$)			Williamson hybrid nanofluid ($\beta \longrightarrow \infty, We = 0.2, \lambda_1 = 0$)		
η	RK4	ADM	DNN	ADM	RK4	DNN	ADM	RK4	DNN
0.0	0.000000	0.000000	0.000000	0.000000	0.000000	0.000000	0.000000	0.000000	0.000000
0.1	0.014371	0.014371	0.014374	0.022976	0.022976	0.022976	0.023872	0.023872	0.023871
0.2	0.025749	0.025749	0.025751	0.041373	0.041373	0.041374	0.043135	0.043135	0.043134
0.3	0.034144	0.034144	0.034146	0.055249	0.055249	0.055249	0.057826	0.057826	0.057825
0.4	0.039520	0.039520	0.039522	0.064540	0.064540	0.064540	0.067851	0.067850	0.067850
0.5	0.041797	0.041797	0.041798	0.069045	0.069045	0.069045	0.072959	0.072959	0.072959
0.6	0.040842	0.040842	0.040843	0.068404	0.068404	0.068405	0.072715	0.072715	0.072716
0.7	0.036468	0.036468	0.036468	0.062076	0.062076	0.062077	0.066455	0.066455	0.066455
0.8	0.028426	0.028426	0.028426	0.049301	0.049301	0.049302	0.053223	0.053222	0.053223
0.9	0.016401	0.016401	0.016401	0.029058	0.029058	0.029058	0.031684	0.031684	0.031684
1.0	0.000000	0.000000	0.000000	0.000000	0.000000	0.000000	0.000000	0.000000	0.000000

Table 3 Comparison of the DNN results of the Nusselt number with the RK4 and ADM values for each case of the fluid model for different Reynolds numbers when $Ha = 2$, $P = 1$, $Pe = 2$ and $Br = 10$

Re	Casson hybrid nanofluid			Eyring-Powell hybrid nanofluid			Williamson hybrid nanofluid		
	ADM	RK4	DNN	ADM	RK4	DNN	ADM	RK4	DNN
0.50	0.76483	0.76483	0.76495	0.82170	0.82170	0.82192	0.82840	0.82840	0.82834
1.00	0.75052	0.75052	0.75029	0.79034	0.79036	0.79045	0.79386	0.79386	0.79393
2.00	0.72276	0.72276	0.72279	0.73238	0.73235	0.73248	0.73018	0.73063	0.73074

mina on the hybrid nanofluid results in increases in the rate of entropy generation and the Bejan number for all the fluids (Casson, Williamson, and Eyring-Powell), as depicted by Fig. 7c and d. The plot in Fig. 8 shows the variation of the Nusselt number (Nu) with respect to the Hartmann number (Ha), which represents the magnetic field strength, for three different non-Newtonian hybrid nanofluids (Casson, Eyring-Powell, and Williamson) at various values of the Reynolds numbers ($Re = 1.0,\ 2.0,\ 3.0$). As the Hartmann number increases, the Nusselt number decreases for all fluid models, indicating that a stronger magnetic field suppresses heat transfer. This behaviour is typical in magnetohydrodynamic (MHD) flows, where the Lorentz force generated by the magnetic field acts to slow down the flow and reduce convective heat transfer. The Casson hybrid nanofluid shows the most favourable heat transfer characteristics, while the Williamson hybrid nanofluid exhibits the least.

Tables 2 and 3 give the approximate solutions obtained using the three methods as various parameters are varied. A good level of consistency in solutions obtained is observed. In Table 2, the velocity profile $f(\eta)$ results from the RK4, Adomian decomposition, and deep neural network methods match up to four decimal places for all values of η presented in the table. Table 3 serves two purposes: it validates the accuracy of the solution methodologies and also presents the Nusselt number values for each fluid as a function of varying Reynolds numbers. It is revealed that the Casson hybrid nanofluid has the least Nusselt number.

Conclusion

This study provided a detailed analysis of the dynamics of three complex fluids flow: Casson, Williamson, and Eyring-Powell within a microchannel. Under varying fluid parameter conditions, the behaviour of a specific complex fluid can be accurately modelled and simulated. This unified approach simplified the deterministic model while accurately capturing the dynamics of each fluid. The investigation focused explicitly on the entropy generation and the influence of a magnetic field, which is incorporated into the momentum and energy conservation equations, allowing for a comprehensive understanding of the fluids' behaviour under magnetohydrodynamic conditions. Two distinct nanoparticles were introduced into the fluid to enhance thermal conductivity and improve heat transfer performance. The fluid model is described within a deterministic framework. Both the deep neural network and Adomian decomposition methods are used for parametric analysis. These two methods were compared with the fourth-order Runge–Kutta (RK4) method to validate their accuracy. The results agreed up to an error of 10^{-6}, as shown in Table 2. The key findings from this study are as follows:

- Increasing the Hartmann number reduces flow velocity, with the Casson fluid exhibiting the lowest flow rate and the Williamson fluid showing the highest. The flow remains symmetric about the mid-line of the microchannel.
- As the Brinkman number increases, the entropy generation rate rises for all fluids, whereas the Bejan number decreases correspondingly for each fluid.
- The nanoparticle volume fraction hinders the fluid flow for all fluids, yet it enhances the thermal distribution profiles and increases the entropy generation rate and the Bejan number. This suggests that while nanoparticles hinder fluid movement, they can significantly improve heat transfer efficiency and overall thermal management within the system.
- As the fluid flow becomes faster (higher Re), both the thermal transport efficiency (as represented by Nu) and the effect of the magnetic field (as indicated by Ha) reduce.
- As the Reynolds number increases by 300% from 0.50, the fluid heat transfer ratio decreases by 5.50% for the Casson hybrid nanofluid, 10.87% for the Eyring-Powell hybrid nanofluid, and 11.86% for the Williamson hybrid nanofluid.

The current model is limited, as only a few thermophysical properties are considered in the dynamical system. However, it can serve as a foundation for future research. Future research will (i) investigate the onset of instability in these hydromagnetic flows, (ii) explore the flow problems in different geometrical configurations, and (iii) examine the impact of non-constant thermophysical properties.

Author Contributions H. A. O: conceptualization, investigation, software, and analysis. Y. O. T.: conceptualization, original writing, analysis, and reviewing. S. D. O: review, analysis, software, editing, and supervision. O.O: review, editing, and supervision. T.M.A: review, editing, and supervision.

Funding Open access funding provided by Rhodes University. This work is based on the research supported in part by the National Research Foundation of South Africa (Ref Number: TTK2204163593).

Data Availability No datasets were generated or analyzed during the current study.

Declarations

Conflict of interest The authors declare no competing interests.

Ethical approval Not applicable.

Open Access This article is licensed under a Creative Commons Attribution 4.0 International License, which permits use, sharing, adaptation, distribution and reproduction in any medium or format, as long as you give appropriate credit to the original author(s) and the source, provide a link to the Creative Commons licence, and indicate if changes were made. The images or other third party material in this article are included in the article's Creative Commons licence, unless indicated otherwise in a credit line to the material. If material is not included in the article's Creative Commons licence and your intended use is not permitted by statutory regulation or exceeds the permitted use, you will need to obtain permission directly from the copyright holder. To view a copy of this licence, visit http://creativecommons.org/licenses/by/4.0/.

References

1. Neužil P, Giselbrecht S, Länge K, Huang TJ, Manz A (2012) Revisiting lab-on-a-chip technology for drug discovery. Nat Rev Drug Discov 11:620–632
2. Yang X, Liu J (2018) Chapter four - advances in liquid metal science and technology in chip cooling and thermal management. Adv Heat Tran 50(Editor(s): Ephraim M. Sparrow, John P. Abraham, John M. Gorman.):187–300
3. Chippada S (1996) Numerical study of thin film flow and open channel flows. Rice University, Department of Mechanical Engineering and Materials Science
4. Ireka IE, Okoya SS (2020) Analysis of unsteady flow of second-grade fluid with power law spatially distributed viscosity. Afrika Mat 31(516):1175–1191. https://doi.org/10.1007/s13370-020-00789-y
5. Chinyoka T (2008) Computational dynamics of a thermally decomposable viscoelastic lubricant under shear. J Fluids Eng 130(12):121201. https://doi.org/10.1115/1.2978993
6. Das S, Karmakar P, Ali A, Patra RR, Jana RN (2024) Shear-driven flow of an ionic fluid in a narrow vertical channel under a hall electric field. Z Angew Math Mech 104:e202301079
7. Nazeer M, Khan MI, Chu YM, Kadry S, Eid MR (2021) Mathematical modeling of multiphase flows of third-grade fluid with lubrication effects through an inclined channel: analytical treatment. Afrika Mat 43(10):1555–1567
8. Das S, Mahato N, Ali A, Jana RN (2023) Aspects of Arrhenius kinetics and hall currents on gyratory Couette flow of magnetized ethylene glycol containing bi-hybridized nanomaterials. Heat Transf 52(4):2995–3026
9. Chhabra RP (2010) Non-Newtonian fluids: an introduction. In: Krishnan J, Deshpande A, Kumar P (eds) Rheology of complex fluids. Springer, New York, NY, vol 10, pp 168
10. Ogunseye HA, Salawu SO, Tijani YO, Riliwan M, Sibanda P (2019) Dynamical analysis of hydromagnetic Brownian and thermophoresis effects of squeezing Eyring-Powell nanofluid flow with variable thermal conductivity and chemical reaction. Multidiscip Model Mater Struct 15(6):1100–1120
11. Sharma KR, Jain S (2024) An unsteady MHD Williamson fluid flow in a vertical porous channel with porous media and thermal radiation. Int J Adv Eng Sci Appl Math 16:274–285
12. Zehra I, Yousaf MM, Nadeem S (2015) Numerical solutions of Williamson fluid with pressure dependent viscosity. Results Phys 5:20–25
13. Titiloye EO, Adeosun AT, Akolade MT, Tijani YO, Olabode JO (2023) Thermal criticality of electromagnetohydrodynamic reactive squeezed Casson material in a combustible channel: a spectral approach. Comput Thermal Sci: Int J 15(4):69–81
14. Fung YC, Skalak R (1981) Biomechanics: mechanical properties of living tissues. J Biomech Eng 103(4):231–298
15. Wajihah SA, Sankar DS (2023) A review on non-Newtonian fluid models for multi-layered blood rheology in constricted arteries. Arch Appl Mech 93:1771–1796
16. Ullah Z, Ullah I, Zaman G, Khan H, Muhammad T (2021) Mathematical modeling and thermodynamics of Prandtl-Eyring fluid with radiation effect: a numerical approach. Sci Rep 11(1):22201
17. Khan Z, Rasheed HU, Abbas T, Khan W, Khan I, Baleanu D, Sooppy-Nisar K (2020) Analysis of Eyring-Powell fluid flow used as a coating material for wire with variable viscosity effect along with thermal radiation and Joule heating. Crystals 10(3):168
18. Patil PM, Goudar B (2023) Impact of impulsive motion on the Eyring-Powell nanofluid flow across a rotating sphere in MHD convective regime: entropy analysis. J Magn Magn Mater 571:170590
19. Kudenatti RB, Noor-E-Misbah (2023) The onset of instability in a hydromagnetic channel flow of Casson fluid: the accurate solutions. Appl Math Comput 436(127475):1–6
20. Qushairi MA, Yeou JL, Shafie S, Khan I, Ismail Z (2008) Exact solution for unsteady free convection flow of Casson fluid in vertical channel. Mater Surf 189(01007):1–6
21. Shashikumar NS, Kumara BCP, Gireesha BJ, Makinde OD (2018) Thermodynamics analysis of MHD Casson fluid slip flow in a porous microchannel with thermal radiation. Diffusion Found 16(120–139):7. https://doi.org/10.4028/www.scientific.net/DF.16.120
22. Shashikumar NS, Madhu M, Sindhu S, Gireesha BJ, Kishan N (2021) Thermal analysis of MHD Williamson fluid flow through a microchannel. Int Commun Heat Mass Transf 127:105582. https://doi.org/10.1016/j.icheatmasstransfer.2021.105582
23. Reddy SRR, Jakeer S, Rupa ML (2023) ANN model of three-dimensional micropolar dusty hybrid nanofluid flow with Coriolis force: biomedical applications. Indian J Phys 97:3801–3825
24. Das S, Sarkar S, Ali A, Jana RN (2024) Exploration of magnetically influenced flow dynamics of a dusty fluid induced by the ramped movement of a thermally active plate. Arch Appl Mech 94:407–433
25. Ali A, Das S, Jana RN (2024) MHD radiant couple stress tetrahybridized nanofluid streaming inside slanted rotating micro-parallel plates subject to Hall currents: a neuro-computing approach. Arch Civil Mech Eng 24:198
26. Sciacovelli A, Verda V, Sciubba E (2015) Entropy generation analysis as a design tool–a review. Renew Sustain Energy Rev 43:1167–1181

27. Manglik RM, Prusa J (1995) Viscous dissipation in non-Newtonian flows - implications for Nusselt number. J Thermophys Heat Transf 9(4):733–742
28. Ogunseye HA, Tijani YO, Sibanda P (2020) Entropy generation in an unsteady Eyring-Powell hybrid nanofluid flow over a permeable surface: a Lie group analysis. Heat Transf 49(6):3374–3390
29. Jakeer S, Bala Anki Reddy P, Basha HT, Reddy SRR (2024) Entropy minimization of the non-Newtonian bio-hybrid (Fe_3O_4-CuO/blood) nanofluid flow over a linear extending sheet by means of induced magnetic field. Int J Mod Phys B 38(10): 2450142
30. Adomian G (1994) Solving frontier problems of physics: the decomposition method. Kluwer Academic Publishers
31. Liao S (2012) Beyond perturbation: introduction to the homotopy analysis method. Chapman andHall/CRC Press, Boca Raton
32. Motsa SS (2013) A new spectral local linearization method for nonlinear boundary layer flow problems. J Appl Math 2013(1):423628. https://onlinelibrary.wiley.com/doi/full/10.1155/2013/423628
33. Lagaris IE, Likas A, Fotiadis DI (1998) Artificial neural networks for solving ordinary and partial differential equations. IEEE Trans Neural Netw 9(5):987–1000
34. Oloniiju SD, Tijani YO, Otegbeye O (2024) Thermal analysis of extended surfaces using deep neural networks. Open Phys 22(1):1–12
35. Reddy SRR, Jakeer S, Sathishkumar VE, Basha HT, Cho J (2024) Numerical study of TC_4-NiCr/eg+ water hybrid nanofluid over a porous cylinder with Thompson and Troian slip boundary condition: artificial neural network model. Case Stud Thermal Eng 53:103794
36. Abdul-Majid W (2009) Partial differential equations and solitary waves theory. Springer, Berlin Heidelberg. https://doi.org/10.1007/978-3-642-00251-9
37. Duan J, Rach R (2011) A new modification of the Adomian decomposition method for solving boundary value problems for higher order nonlinear differential equations. Appl Math Comput 218(8):4090–4118. https://doi.org/10.1016/j.amc.2011.09.037
38. Ogunseye HA, Sibanda P (2019) A mathematical model for entropy generation in a Powell-Eyring nanofluid flow in a porous channel. Heliyon 5(5):e01662. https://doi.org/10.1016/j.heliyon.2019.e01662
39. Giwa SO, Sharifpur M, Meyer JP (2020) Effects of uniform magnetic induction on heat transfer performance of aqueous hybrid ferrofluid in a rectangular cavity. Appl Thermal Eng 170:115004. https://doi.org/10.1016/j.applthermaleng.2020.115004
40. Aly EH, Pop I (2019) MHD flow and heat transfer over a permeable stretching/shrinking sheet in a hybrid nanofluid with a convective boundary condition. Int J Numer Methods Heat Fluid Flow 28:3012–3038. https://doi.org/10.1108/HFF-12-2018-0794
41. Kumar KA, Sandeep N, Sugunamma V, Animasaun IL (2020) Effect of irregular heat source/sink on the radiative thin film flow of MHD hybrid ferrofluid. J Therm Anal Calorim 139:2145–2153. https://doi.org/10.1007/s10973-019-08628-4
42. López A, Ibáñez G, Pantoja J, Moreira J, Lastres O (2017) Entropy generation analysis of MHD nanofluid flow in a porous vertical microchannel with nonlinear thermal radiation, slip flow and convective-radiative boundary conditions. Int J Heat Mass Transf 107:982–994
43. Bejan A (2013) Entropy generation minimization: the method of thermodynamic optimization of finite-size systems and finite-time processes. CRC Press
44. Raissi M, Perdikaris P, Karniadakis GE (2019) Physics-informed neural networks: a deep learning framework for solving forward and inverse problems involving nonlinear partial differential equations. J Comput Phys 378:686–707. https://doi.org/10.1016/j.jcp.2018.10.045
45. Liu DC, Nocedal J (1989) On the limited memory BFGS method for large scale optimization. Math Program 45(1):503–528
46. Zubov K, McCarthy Z, Ma Y, Calisto F, Pagliarino V, Azeglio S, Bottero L, Luján E, Sulzer V, Bharambe A, Vinchhi N, Balakrishnan K, Upadhyay D, Rackauckas C (2021) NeuralPDE: automating physics-informed neural networks (PINNs) with error approximations
47. Adomian G (1994) The decomposition method. – solving frontier problems of physics. Kluwer, Boston, MA, vol 1, pp 139476
48. Adesanya SO, Ogunseye HA, Jangili S (2018) Unsteady squeezing flow of a radiative Eyring-Powell fluid channel flow with chemical reactions. Int J Thermal Sci 125:440–447

Publisher's Note Springer Nature remains neutral with regard to jurisdictional claims in published maps and institutional affiliations.